Journal of Materials Chemistry A

ROYAL SOCIETY OF CHEMISTRY

PAPER

View Article Online
View Journal | View Issue

Cite this: J. Mater. Chem. A, 2021, 9, 9301

A 2D MOF-based artificial light-harvesting system with chloroplast bionic structure for photochemical catalysis†

Zhong Wei Jiang,[a] Ting Ting Zhao,[a] Shu Jun Zhen,[a] Chun Mei Li,[b] Yuan Fang Li *[a] and Cheng Zhi Huang *[ab]

Received 11th February 2021
Accepted 16th March 2021

DOI: 10.1039/d1ta01278a

rsc.li/materials-a

Developing an efficient artificial light-harvesting system (ALHS) with high solar spectrum overlap, energy transfer efficiency and photocatalytic performance remains a key challenge to realize sustainable energy utilization. Inspired by nature, herein, a 2D ALHS, namely, 2D MB/Yb-TCPP-SO_4 nanosheets with chloroplast bionic structure were successfully constructed by coupling a kind of porphyrin-based 2D lanthanide metal–organic framework (namely, Yb-TCPP MOF) and methylene blue (MB). The newly assembled 2D ALHS showed 100% spectrum efficiency in the visible light region and high-efficiency energy transfer (up to 78.6%) between 2D Yb-TCPP nanosheets and MB. Significantly, this 2D ALHS possessed high activity towards the photocatalytic semi-synthesis of artemisinin after installing Brønsted acid sites, giving a record yield as high as 85%. This demonstrated that the as-constructed 2D ALHS is an ideal artificial solar converter, which showed a promising application for photochemical catalysis.

Introduction

Light-harvesting systems in natural photosynthesis have attracted much research interests on account of the efficient solar energy conversion and utilization for promoting sustainable development.[1–4] In natural photosynthesis, chloroplast, a highly integrated energy converter in plants and some photosynthetic bacteria, contains tightly stacked sheet-like thylakoids to capture light energy, followed by a photoinduced energy transfer to the reaction center, thus realizing the conversion of light energy into chemical energy.[5–8] A variety of sophisticated bionic platforms, such as dendrimers,[9,10] gels,[11–14] biohybrid assemblies,[15–18] DNA[19] and supramolecules with aggregation induced emission hosts[20–23] have been successfully developed to mimic these natural light-harvesting systems. Although these 0D, 1D or 3D ALHSs with ingenious design have achieved light-harvesting, they suffer from insufficient light harvesting in visible areas and inefficient energy transfer. Furthermore, the utilization of the harvested light energy by ALHS for photocatalytic reaction to promote matter conversion remains less addressed.

In recent years, chemists have found that chromophores in crystal MOFs are close to each other rather than in direct contact, effectively avoiding the aggregation-caused quenching by the close arrangement of chromophores, and the highly ordered chromophores within MOF crystals contribute to photon capture and energy transfer.[24–29] However, the transfer of internal energy within conventional 3D bulk MOF crystals to external acceptors is severely limited by the energy transfer distance constraints, thus restraining the energy transfer efficiency and photocatalytic performance. 2D materials with extraordinary physicochemical properties have been widely used in photocatalysis.[30–32] 2D MOFs, as newly developed 2D materials, have been widely used in electronics,[33] optics,[34–36] catalysis,[37] sensing,[38] medical science,[39,40] as well as in gas storage and separation.[41,42] Compared with 3D bulk MOFs, 2D MOFs can efficiently transfer the captured energy to external acceptors as each chromophore molecule on the 2D nanosheet is located on the exposed outer surface close to the acceptors. Furthermore, 2D MOFs have a larger specific surface area and more accessible active sites, which can provide abundant reactive sites and high mass transfer rate for boosting the photocatalytic performance.[43,44]

Herein, porphyrin-based 2D lanthanide MOFs, namely 2D Yb-TCPP nanosheets,[45] were used as scaffolds to construct a 2D MOF-based ALHS. Just as sheet-like thylakoids in chloroplasts that are packed tightly together to increase the surface area for light-harvesting, 2D Yb-TCPP nanosheets contain individual porphyrin structural units that can be assembled together to form a high surface area array for photon collection. Therefore, 2D Yb-TCPP nanosheets can be used as ideal scaffolds for

[a]Key Laboratory of Luminescence Analysis and Molecular Sensing, Ministry of Education, College of Chemistry and Chemical Engineering, Southwest University, Chongqing 400715, P. R. China. E-mail: chengzhi@swu.edu.cn; liyf@swu.edu.cn

[b]Key Laboratory of Luminescence and Real-Time Analysis System, Chongqing Science and Technology Bureau, College of Pharmaceutical Sciences, Southwest University, Chongqing 400715, P. R. China

† Electronic supplementary information (ESI) available: Detailed experimental procedures, characterization and additional figures and tables. See DOI: 10.1039/d1ta01278a

mimicking chloroplasts due to the similar structural units to thylakoids and orderly arranged porphyrin pigment molecules to simulate chlorophyll. To better mimic natural photosynthesis and make full use of the harvested energy, a photosensitizer, MB, acting as the energy receptor was coupled to 2D Yb-TCPP nanosheets so as to construct the 2D MB/Yb-TCPP-SO_4 ALHS, which structurally resembled the thylakoids in natural chloroplasts. The coupled MB effectively improved the solar spectrum efficiency of 2D Yb-TCPP nanosheets, and the efficient Förstor resonance energy transfer (FRET) between Yb-TCPP and MB greatly increased the energy utilization to boost the $^1O_2$ generation *via* a synergistic effect. Significantly, by treating with acids to install Brønsted acid sites, the 2D MB/Yb-TCPP-HSO_4 ALHS showed a high photocatalytic activity for the semi-synthesis of artemisinin, giving the highest yield of 85% among all known photooxidation processes of dihydroartemisinic acid up to now (Scheme 1).

Results and discussion

The excellent spectral overlap between 2D Yb-TCPP nanosheet emission and MB absorption spectra was crucial to allow effective coupling for FRET (Fig. 1a). To efficiently integrate the 2D Yb-TCPP nanosheets and MB together, the strategy of electrostatic self-assembly was applied (Fig. 1b). The SDS-modified 2D Yb-TCPP nanosheets (Yb-TCPP-SO_4) with strong electronegativity were able to efficiently adsorb the electropositive MB. The electronegativity of the nanosheets decreased with the increase in the MB adsorption concentration, and did not change significantly when the adsorption equilibrium was reached (Fig. 2a). The absorption band around 665 nm of MB was observed distinctly in the absorption spectrum of MB/Yb-TCPP-SO_4, and it increased with the increase in the MB loading (Fig. 2b). The saturated adsorption capacity of MB was calculated to be 60 μg mg^{-1} by comparing the UV-vis absorbance to the calibration curve (Fig. S1†). Correspondingly, the fluorescence emission of 2D Yb-TCPP nanosheets decreased with the increase in the MB adsorption (Fig. 2c). To understand the quenching mechanism clearly, the fluorescence decay curves of

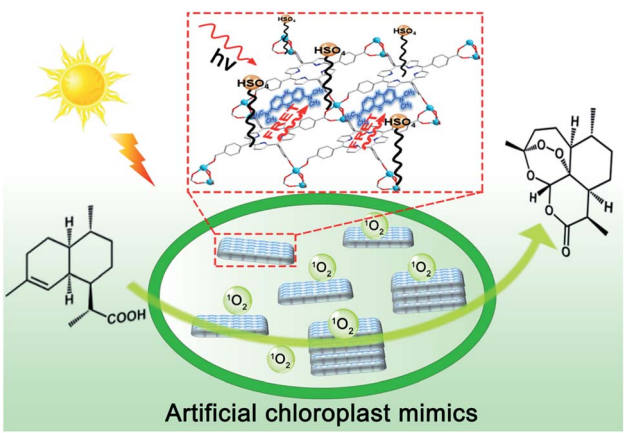

Scheme 1 Working principle of the constructed 2D ALHS with chloroplast bionic structure for artemisinin production.

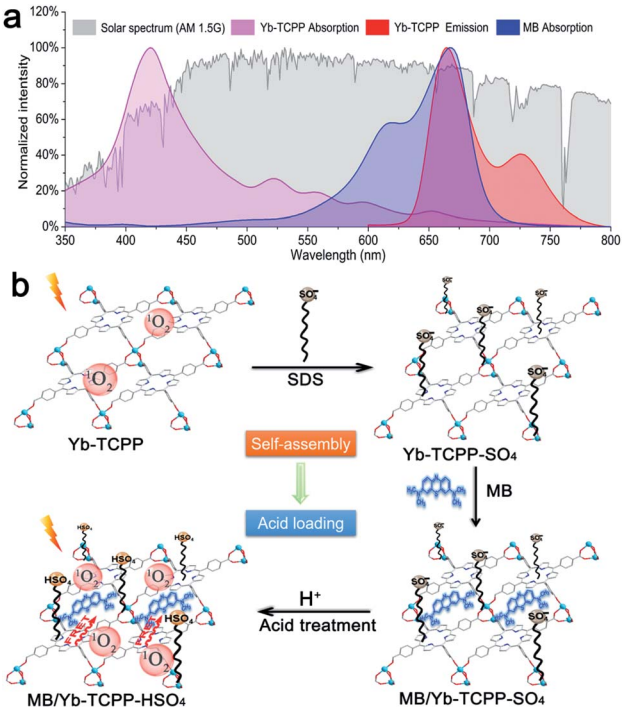

Fig. 1 Experimental design for fabricating 2D MB/Yb-TCPP-SO_4 and MB/Yb-TCPP-HSO_4 nanosheets. (a) The spectral overlap of Yb-TCPP and MB; (b) scheme for electrostatic self-assembly of Yb-TCPP and MB.

2D Yb-TCPP nanosheets were measured before and after MB loading. Obviously, the fluorescence lifetime of 2D Yb-TCPP nanosheets got shortened with the formation of MB/Yb-TCPP-

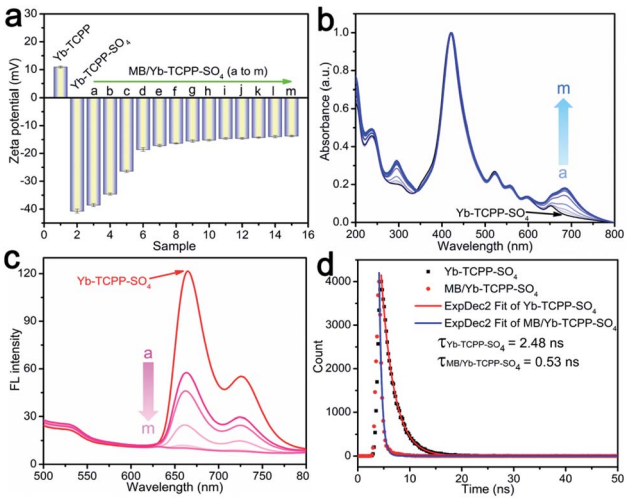

Fig. 2 The zeta potential and spectral characterization of SDS-modified 2D Yb-TCPP nanosheets (Yb-TCPP-SO_4) with MB loading. (a) The zeta potential of 2D Yb-TCPP nanosheets, Yb-TCPP-SO_4 and MB/Yb-TCPP-SO_4 with different MB loadings (from a to m); (b) the absorption spectra and (c) corresponding fluorescence spectra of MB/Yb-TCPP-SO_4 with different MB loadings (from a to m); (d) time-resolved fluorescence decay traces of Yb-TCPP-SO_4 and MB/Yb-TCPP-SO_4.

SO_4, demonstrating that fluorescence quenching was ascribed to the occurrence of FRET (Fig. 2d). In the meantime, the FRET efficiency was calculated as high as 78.6% due to its open 2D plane structure and relatively close distance between the 2D Yb-TCPP nanosheets and MB.

The peaks at 1068 cm^{-1}, 1142 cm^{-1} and 1338 cm^{-1} in the FTIR spectra were assigned to the ν(C–S–C), δ(C–N) and ν(C–N, in N–CH_3) vibrations of MB,[46] respectively, which were also present in that of MB/Yb-TCPP-SO_4 (Fig. S2†). Meanwhile, the bands at 500 cm^{-1}, 1036 cm^{-1}, 1394 cm^{-1} and 1625 cm^{-1} assigned to δ(C–N–C), ν(C–S–C), γ(C–H, CH_3) and ν(C–C, ring) of MB, respectively, were also observed in the Raman spectrum of MB/Yb-TCPP-SO_4 (Fig. S3†).[47] The scanning electron microscopy (SEM), transmission electron microscopy (TEM), and atomic force microscopy (AFM) images manifested that MB/Yb-TCPP-SO_4 kept the sheet-like 2D structure of the as-synthesized Yb-TCPP with the thickness of around 1.93 nm (Fig. 3a, b and S4, S5†). Compared to 2D Yb-TCPP nanosheets (Fig. S6†), the thickness increased obviously, indicating that SDS and MB were successfully modified to the surface of 2D Yb-TCPP nanosheets. Moreover, the PXRD patterns of 2D MB/Yb-TCPP-SO_4 nanosheets were consistent with that of 2D Yb-TCPP nanosheets, indicating no structural disruption by surface interaction (Fig. 3c). The similar TGA curves revealed the high thermal stability (up to 400 °C) of 2D MB/Yb-TCPP-SO_4 nanosheets like that of 2D Yb-TCPP nanosheets (Fig. S7†). Significantly, the Brunauer–Emmett–Teller (BET) surface area and pore size distribution of 2D MB/Yb-TCPP-SO_4 nanosheets were also almost identical to that of 2D Yb-TCPP nanosheets, demonstrating that the large surface area and abundant accessible active sites were maintained (Fig. 3d and S8†). All the above results demonstrated that MB was successfully loaded on 2D Yb-TCPP nanosheets through electrostatic self-assembly to form a 2D ALHS that structurally resembled the thylakoids in natural chloroplasts.

To endow 2D MB/Yb-TCPP-SO_4 nanosheets with versatility, we carried out acid treatment to install Brønsted acid sites for facilitating acid catalytic processes. Herein, the as-prepared 2D MB/Yb-TCPP-SO_4 nanosheets were immersed in acid solution such as H_2SO_4, HCl, HNO_3 and trifluoroacetic acid (TFA) to protonate the –SO_4 group that originated from SDS, followed by freeze drying and vacuum drying. The acidity of 2D MB/Yb-TCPP-HSO_4 nanosheets was evaluated by ^{31}P magic-angle spinning (MAS) solid-state NMR spectroscopy (^{31}P MAS NMR).[48,49] For 2D MB/Yb-TCPP-SO_4 nanosheets and 2D MB/Yb-TCPP-HSO_4 nanosheets, the resonances observed below 62 ppm were attributed to the physisorbed and trapped free TMPO in the MOF pores (Fig. S9†).[50,51] The new resonances appeared within the range from 62 to 73 ppm in the spectrum of 2D MB/Yb-TCPP-HSO_4 nanosheets, which were assigned to TMPO adsorbed on the strong Brønsted acid sites, demonstrating the strong acidity of 2D MB/Yb-TCPP-HSO_4 nanosheets.[49,50] Besides, the pH of the washing solution of 2D MB/Yb-TCPP-HSO_4 nanosheets was around 2.20, close to the pK_{a2} value (1.92) of sulfuric acid,[49] indicating the successful protonation of the –SO_4 group (Table S1†). Furthermore, the PXRD patterns showed that the crystal structure was maintained after acidification, demonstrating that 2D MB/Yb-TCPP-HSO_4 nanosheets possess high stability (Fig. S10†).

To evaluate the photoactivity of the newly developed 2D ALHS, UV/vis diffuse reflectance spectroscopy was performed first. 2D MB/Yb-TCPP-SO_4 nanosheets and 2D MB/Yb-TCPP-

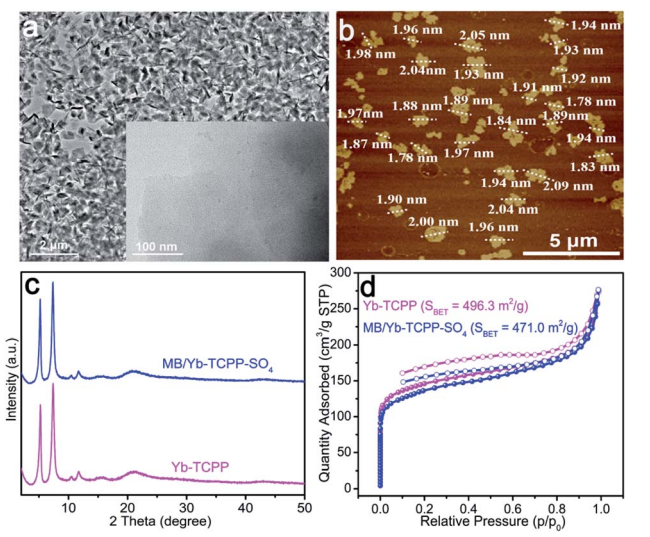

Fig. 3 The characterization of 2D MB/Yb-TCPP-SO_4 nanosheets. (a) TEM and (b) AFM images of the as-synthesized 2D MB/Yb-TCPP-SO_4 nanosheets, inset: high magnification image. (c) PXRD patterns of 2D Yb-TCPP nanosheets and 2D MB/Yb-TCPP-SO_4 nanosheets. (d) N_2 sorption–desorption isotherms of 2D Yb-TCPP nanosheets and 2D MB/Yb-TCPP-SO_4 nanosheets.

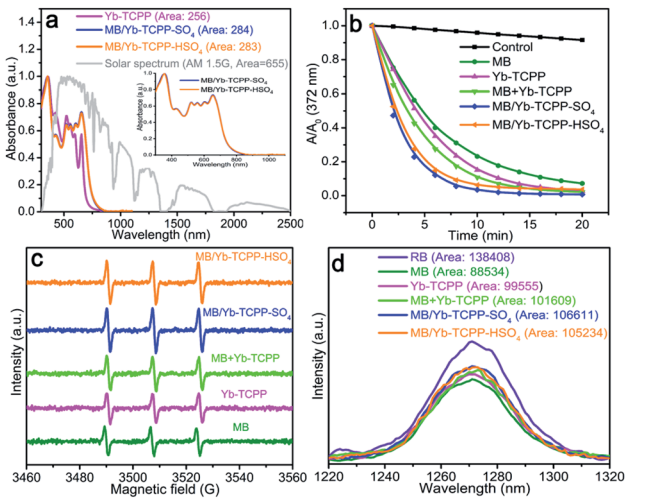

Fig. 4 The photochemical properties of the as-prepared 2D ALHS. (a) UV-vis diffuse reflection spectra of 2D Yb-TCPP nanosheets and 2D MB/Yb-TCPP nanosheets; (b) absorbance decays of DPA (40 mg mL^{-1}) at 372 nm in the presence of MB, Yb-TCPP, MB+Yb-TCPP, 2D MB/Yb-TCPP-SO_4 nanosheets and 2D MB/Yb-TCPP-HSO_4 nanosheets, respectively; (c) the ESR spectra of the different reaction systems in the presence of TEMP under visible-light irradiation; (d) the $^1O_2$ emissions at around 1270 nm induced by MB, 2D Yb-TCPP nanosheets, MB+Yb-TCPP, 2D MB/Yb-TCPP-SO_4 nanosheets, 2D MB/Yb-TCPP-HSO_4 nanosheets and RB in ethanol solution under an excitation of 532 nm.

HSO_4 nanosheets with a theoretical solar spectrum efficiency of 43% (Fig. 4a), where the visible light region accounts for about 43% of the total solar spectrum,[52] offered the ability to fully capture the solar power in the visible light region. The corresponding optical band gap was calculated to be 1.66 eV by Tauc plot, lower than that of 2D Yb-TCPP nanosheets (1.78 eV), further revealing the preferable visible light harvesting capability of 2D MB/Yb-TCPP-SO_4 nanosheets and 2D MB/Yb-TCPP-HSO_4 nanosheets (Fig. S11†). As is well known, porphyrin-based MOFs and MB as photosensitizers can produce singlet oxygen ($^1O_2$) under light irradiation. Therefore, the photochemical activity of the as-constructed 2D ALHS to generate $^1O_2$ was evaluated by using 9,10-diphenylanthracene (DPA) as the $^1O_2$ indicator. The characteristic absorption and emission of DPA decreased with the increase of MB loading under the same reaction conditions, indicating that the higher the loading of MB, the stronger the ability to generate $^1O_2$ (Fig. S12†).

In such cases, the degradation rates of DPA resulting from 2D MB/Yb-TCPP-SO_4 nanosheets were the fastest among the investigated 2D ALHSs, while only a slight change was observed without the presence of photocatalysts (Fig. 4b and S13†). Compared with 2D MB/Yb-TCPP-SO_4 nanosheets, the photocatalytic activity of 2D MB/Yb-TCPP-HSO_4 nanosheets decreased slightly due to the influence of acid. Besides, the electron spin resonance (ESR) spectra of 2D MB/Yb-TCPP-SO_4 nanosheets and 2D MB/Yb-TCPP-HSO_4 nanosheets showed typical 1 : 1 : 1 triplet signals of 4-oxo-TEMPO, and were stronger than that of 2D Yb-TCPP nanosheets, Yb-TCPP+MB and MB, suggesting the stronger ability to produce $^1O_2$ (Fig. 4c). The $^1O_2$ quantum yield was measured by using Rose Bengal (RB) as a standard photosensitizer, and the $^1O_2$ quantum yield was calculated to be 0.55, 0.62, 0.63, 0.66 and 0.65 for MB, 2D Yb-TCPP nanosheets, Yb-TCPP+MB and 2D MB/Yb-TCPP-SO_4 nanosheets and 2D MB/Yb-TCPP-HSO_4 nanosheets, respectively (Fig. 4d and Table S2†). Based on the above results, we concluded that the high activity of the 2D ALHS for the generation of $^1O_2$ can be attributed to the energy transfer-induced synergistic effect between MB and Yb-TCPP.

Photocatalytic semi-synthesis of artemisinin from available artemisinic acid has been considered as an effective approach to minimize the cost of artemisinin extraction or total synthesis.[53–56] In the photooxidation process, the conversion of dihydroartemisinic acid to artemisinin generally undergoes complex oxidation/rearrangements including the peroxidation *via* $^1O_2$-induced Schenck ene reaction, followed by an acid-induced Hock cleavage, a subsequent oxygenation and cyclization to give the final product, artemisinin (Fig. S14†).[54,57,58] Herein, inspired by the exciting features of $^1O_2$ generation and strong Brønsted acid sites, we conducted the photocatalytic synthesis of artemisinin by using the newly developed 2D MB/Yb-TCPP-HSO_4 nanosheets as a biomimetic photocatalytic system. The product was identified as artemisinin by ^1H NMR spectroscopy and mass spectroscopy (Fig. S15–S20†). Surprisingly, 2D MB/Yb-TCPP-HSO_4 nanosheets treated with 0.005 M H_2SO_4 achieved 85% conversion and 41% yield within 0.5 h, and obtained 98% conversion and 85% yield after a reaction for 3 h (Fig. S21† and Table 1, entry 8). Meanwhile, 2D MB/Yb-TCPP-SO_4 treated with other acids also achieved almost 99% conversion and more than 80% yield (Table 1, entries 10, 11, and 12). A big progress could be highlighted as compared to other reported catalytic systems, which gave the yield of artemisinin almost below 70%.[55,56,58–61]

Table 1 Photocatalytic synthesis of artemisinin using different photocatalysts in dichloromethane

Entry	Catalyst	Conversion[e] (%)	Yield[e] (%)
1	MB+TFA	70	36
2	Yb-TCPP+TFA	99	36
3	Yb-TCPP+MB+TFA	99	44
4	MB/Yb-TCPP-SO_4+TFA	99	63
5	Yb-TCPP-HSO_4	99	57
6	MB/Yb-TCPP-HSO_4-0.001M[a]	98	61
7	MB/Yb-TCPP-HSO_4-0.002M[a]	99	79
8	MB/Yb-TCPP-HSO_4-0.005M[a]	98	85
9	MB/Yb-TCPP-HSO_4-0.01M[a]	99	83
10	MB/Yb-TCPP-HSO_4-0.01M[b]	99	83
11	MB/Yb-TCPP-HSO_4-0.01M[c]	99	81
12	MB/Yb-TCPP-HSO_4-0.01M[d]	98	83

[a] Treatment with H_2SO_4. [b] Treatment with HNO_3. [c] Treatment with HCl. [d] Treatment with TFA. [e] Reaction conversions and yields were determined by ^1H NMR spectroscopy using biphenyl as an internal standard.

As previously reported, the low yield of intermediates in peroxidation and cyclization steps limited the conversion yield.[62] To clearly understand the mechanism behind the exceptional activity of 2D MB/Yb-TCPP-HSO_4 nanosheets towards photocatalytic synthesis of artemisinin, we monitored the yields of intermediates 1 and 2 in the photocatalytic process. Under visible light irradiation and in the presence of O_2 but without the addition of an acid, the yields of intermediate 1 were obtained to be 18%, 21%, 22%, 25% for MB, 2D Yb-TCPP nanosheets, MB+Yb-TCPP and 2D MB/Yb-TCPP-SO_4 nanosheets, respectively (Fig. S22†), indicating that the higher quantum yield and faster generation rate of $^1O_2$ are critical to inhibit the formation of byproducts (intermediate 2) in the Schenck ene reaction, thus boosting the formation efficiency of intermediate 1. Besides, acid plays an important role in the Hock cleavage step in the process of photocatalytic synthesis of artemisinin. Usually, TFA was used for inducing acid-catalyzed Hock cleavage of intermediate 1.[58–60] However, a series of dehydration condensation reactions in the cyclization step were carried out,[60,63,64] wherein TFA might not participate effectively. Interestingly, the sulfuric acid (–HSO_4) and sulfonic acid (–HSO_3) groups are commonly used in carbohydrate dehydration condensation reactions.[65–69] That is, –HSO_4 or –HSO_3 may effectively promote the efficiency in the final ring closure step. Verified by comparing to 2D MB/Yb-TCPP-SO_4 nanosheets with the addition of TFA (Table 1, entry 4), 2D MB/Yb-TCPP-HSO_4 nanosheets gave higher yield of artemisinin, manifesting that the formed –HSO_4 not only can be used as Brønsted acid to facilitate Hock cleavage, but also as a dehydrating agent to effectively improve the dehydration cyclization efficiency in the cyclization steps. Thus, the high yield of artemisinin obtained by using 2D MB/Yb-TCPP-HSO_4 nanosheets is due to the energy

transfer-induced synergistic effect for boosting $^1O_2$ generation and abundant $-HSO_4$ groups as Brønsted acid sites, which can effectively accelerate the peroxidation and Hock cleavage, as well as the cyclization, thus giving a record yield as high as 85%.

Recyclability and stability are vital performance metrics of heterogeneous catalytic systems. The photocatalytic activity test demonstrated that the yield decreased slightly after three cycles, but the yield could be recovered after an acid treatment again (Fig. S23†), suggesting that 2D MB/Yb-TCPP-HSO_4 nanosheets possessed high recyclability and regeneration ability. Besides, the PXRD patterns confirmed that the structural integrity of 2D MB/Yb-TCPP-HSO_4 nanosheets were well retained after photocatalysis (Fig. S24†). Furthermore, the long-term stability of 2D MB/Yb-TCPP-HSO_4 nanosheets in water and dichloromethane was monitored by UV-vis absorption spectroscopy, with no MB being observed in the supernatants, indicating no MB leaching (Fig. S25†).

Conclusions

In summary, we have successfully developed a 2D MOF-based ALHS to mimic chloroplast *via* a facile, general, and effective electrostatic self-assembly strategy. The as-constructed 2D MOF-based ALHS with similar structure to the natural chloroplast exhibited a 100% theoretical solar spectrum efficiency in the visible light region and a high-efficiency FRET to boost $^1O_2$ generation. Furthermore, the 2D MOF-based ALHS installed with Brønsted acid sites showed a high photocatalytic activity towards artemisinin semi-synthesis. This study highlights a great potential of 2D MOF-based ALHSs for solar light-harvesting and photocatalytic applications.

Conflicts of interest

The authors declare no competing financial interest.

Acknowledgements

This work was financially supported by the Natural Science Foundation of China (NSFC, no. 21535006, 21874109) and the Fundamental Research Funds for the Central Universities (XDJK2020TY001).

References

1 P. D. Frischmann, K. Mahata and F. Würthner, *Chem. Soc. Rev.*, 2013, **42**, 1847–1870.
2 N. E. Holt, D. Zigmantas, L. Valkunas, X.-P. Li, K. K. Niyogi and G. R. Fleming, *Science*, 2005, **307**, 433–436.
3 Y. Jiang and J. McNeill, *Chem. Rev.*, 2016, **117**, 838–859.
4 O. Stroyuk, A. Raevskaya and N. Gaponik, *Chem. Soc. Rev.*, 2018, **47**, 5354–5422.
5 R. Croce and H. van Amerongen, *Nat. Chem. Biol.*, 2014, **10**, 492–501.
6 G. D. Scholes and G. R. Fleming, *Adv. Chem. Phys.*, 2005, **132**, 57–129.
7 J. F. Allen, W. B. M. d. Paula, S. Puthiyaveetil and J. Nield, *Trends Plant Sci.*, 2011, **16**, 645–655.
8 T. Pfannschmidt, *Trends Plant Sci.*, 2003, **8**, 33–41.
9 Y.-H. Jeong, M. Son, H. Yoon, P. Kim, D.-H. Lee, D. Kim and W.-D. Jang, *Angew. Chem., Int. Ed.*, 2014, **53**, 6925–6928.
10 W.-Q. Wu, H.-L. Feng, H.-S. Rao, Y.-F. Xu, D.-B. Kuang and C.-Y. Su, *Nat. Commun.*, 2014, **5**, 3968.
11 R. Sethy, J. Kumar, R. Métivier, M. Louis, K. Nakatani, N. M. T. Mecheri, A. Subhakumari, K. G. Thomas, T. Kawai and T. Nakashima, *Angew. Chem., Int. Ed.*, 2017, **56**, 15053–15057.
12 C. Felip-León, S. Díaz-Oltra, F. Galindo and J. F. Miravet, *Chem. Mater.*, 2016, **28**, 7964–7972.
13 P. Duan, N. Yanai, H. Nagatomi and N. Kimizuka, *J. Am. Chem. Soc.*, 2015, **137**, 1887–1894.
14 A. Ajayaghosh, V. K. Praveen, C. Vijayakumar and S. J. George, *Angew. Chem., Int. Ed.*, 2007, **46**, 6260–6265.
15 Q. Zou, K. Liu, M. Abbas and X. Yan, *Adv. Mater.*, 2016, **28**, 1031–1043.
16 X. Li, S. Qiao, L. Zhao, S. Liu, F. Li, F. Yang, Q. Luo, C. Hou, J. Xu and J. Liu, *ACS Nano*, 2019, **13**, 1861–1869.
17 L. Zhao, H. Zou, H. Zhang, H. Sun, T. Wang, T. Pan, X. Li, Y. Bai, S. Qiao, Q. Luo, J. Xu, C. Hou and J. Liu, *ACS Nano*, 2017, **11**, 938–945.
18 H. Kashida, H. Azuma, R. Maruyama, Y. Araki, T. Wada and H. Asanuma, *Angew. Chem., Int. Ed.*, 2020, **59**, 11360–11363.
19 H. Kashida, H. Azuma, R. Maruyama, Y. Araki, T. Wada and H. Asanuma, *Angew. Chem.*, 2020, **132**, 11456–11459.
20 X. M. Chen, Q. Cao, H. K. Bisoyi, M. Wang, H. Yang and Q. Li, *Angew. Chem., Int. Ed.*, 2020, **59**, 10493–10497.
21 M. Hao, G. Sun, M. Zuo, Z. Xu, Y. Chen, X.-Y. Hu and L. Wang, *Angew. Chem., Int. Ed.*, 2020, **59**, 10095–10100.
22 J.-J. Li, Y. Chen, J. Yu, N. Cheng and Y. Liu, *Adv. Mater.*, 2017, **29**, 1701905.
23 D. Zhang, W. Yu, S. Li, Y. Xia, X. Li, Y. Li and T. Yi, *J. Am. Chem. Soc.*, 2021, **143**, 1313–1317.
24 H. J. Son, S. Jin, S. Patwardhan, S. J. Wezenberg, N. C. Jeong, M. So, C. E. Wilmer, A. A. Sarjeant, G. C. Schatz, R. Q. Snurr, O. K. Farha, G. P. Wiederrecht and J. T. Hupp, *J. Am. Chem. Soc.*, 2013, **135**, 862–869.
25 J.-L. Wang, C. Wang and W. Lin, *ACS Catal.*, 2012, **2**, 2630–2640.
26 J. Yu, X. Li and P. Deria, *ACS Sustainable Chem. Eng.*, 2018, **7**, 1841–1854.
27 C. Y. Lee, O. K. Farha, B. J. Hong, A. A. Sarjeant, S. T. Nguyen and J. T. Hupp, *J. Am. Chem. Soc.*, 2011, **133**, 15858–15861.
28 X. Li, J. Yu, D. J. Gosztola, H. C. Fry and P. Deria, *J. Am. Chem. Soc.*, 2019, **141**, 16849–16857.
29 T. Zhang and W. Lin, *Chem. Soc. Rev.*, 2014, **43**, 5982–5993.
30 B. Zhang, T. Fan, N. Xie, G. Nie and H. Zhang, *Adv. Sci.*, 2019, **6**, 1901787.
31 W. Han, C. Zang, Z. Huang, H. Zhang, L. Ren, X. Qi and J. Zhong, *Int. J. Hydrogen Energy*, 2014, **39**, 19502–19512.
32 C. Tan, X. Cao, X. J. Wu, Q. He, J. Yang, X. Zhang, J. Chen, W. Zhao, S. Han, G. H. Nam, M. Sindoro and H. Zhang, *Chem. Rev.*, 2017, **117**, 6225–6331.

33 X. Song, J. Liu, T. Zhang and L. Chen, *Sci. China: Chem.*, 2020, **63**, 1391–1401.
34 X. Jiang, L. Zhang, S. Liu, Y. Zhang, Z. He, W. Li, F. Zhang, Y. Shi, W. Lü, Y. Li, Q. Wen, J. Li, J. Feng, S. Ruan, Y.-J. Zeng, X. Zhu, Y. Lu and H. Zhang, *Adv. Opt. Mater.*, 2018, **6**, 1800561.
35 Z. Sun, X. Jiang, Q. Wen, W. Li and H. Zhang, *J. Mater. Chem. C*, 2019, **7**, 4662–4666.
36 J. He, L. Tao, H. Zhang, B. Zhou and J. Li, *Nanoscale*, 2019, **11**, 2577–2593.
37 A. Dhakshinamoorthy, A. M. Asiri and H. Garcia, *Adv. Mater.*, 2019, **31**, 1900617.
38 M. V. Varsha and G. Nageswaran, *J. Electrochem. Soc.*, 2020, **167**, 136502.
39 K. Lu, C. He and W. Lin, *J. Am. Chem. Soc.*, 2014, **136**, 16712–16715.
40 C. He, K. Lu, D. Liu and W. Lin, *J. Am. Chem. Soc.*, 2014, **136**, 5181–5184.
41 Y. Peng and W. Yang, *Adv. Opt. Mater.*, 2019, **7**, 1901514.
42 P. Chandrasekhar, A. Mukhopadhyay, G. Savitha and J. N. Moorthy, *J. Mater. Chem. A*, 2017, **5**, 5402–5412.
43 M. Zhao, Y. Huang, Y. Peng, Z. Huang, Q. Ma and H. Zhang, *Chem. Soc. Rev.*, 2018, **47**, 6267–6295.
44 M. Zhao, Q. Lu, Q. Ma and H. Zhang, *Small Methods*, 2017, **1**, 1600030.
45 Z. W. Jiang, Y. C. Zou, T. T. Zhao, S. J. Zhen, Y. F. Li and C. Z. Huang, *Angew. Chem., Int. Ed.*, 2020, **59**, 3300–3306.
46 O. V. Ovchinnikov, A. V. Evtukhova, T. S. Kondratenko, M. S. Smirnov, V. Y. Khokhlov and O. V. Erina, *Vib. Spectrosc.*, 2016, **86**, 181–189.
47 P. H. B. Aoki, D. Volpati, W. Caetano and C. J. L. Constantino, *Vib. Spectrosc.*, 2010, **54**, 93–102.
48 W. Peng, J. Mi, F. Liu, Y. Xiao, W. Chen, Z. Liu, X. Yi, W. Liu and A. Zheng, *ACS Catal.*, 2020, **10**, 11848–11856.
49 C. A. Trickett, T. M. Osborn Popp, J. Su, C. Yan, J. Weisberg, A. Huq, P. Urban, J. Jiang, M. J. Kalmutzki, Q. Liu, J. Baek, M. P. Head-Gordon, G. A. Somorjai, J. A. Reimer and O. M. Yaghi, *Nat. Chem.*, 2018, **11**, 170–176.
50 J. Jiang, F. Gandara, Y. B. Zhang, K. Na, O. M. Yaghi and W. G. Klemperer, *J. Am. Chem. Soc.*, 2014, **136**, 12844–12847.
51 A. Zheng, S. J. Huang, S. B. Liu and F. Deng, *Phys. Chem. Chem. Phys.*, 2011, **13**, 14889–14901.
52 N. Roslan, M. E. Ya'acob, M. A. M. Radzi, Y. Hashimoto, D. Jamaludin and G. Chen, *Renewable Sustainable Energy Rev.*, 2018, **92**, 171–186.
53 C. J. Paddon, P. J. Westfall, D. J. Pitera, K. Benjamin, K. Fisher, D. McPhee, M. D. Leavell, A. Tai, A. Main, D. Eng, D. R. Polichuk, K. H. Teoh, D. W. Reed, T. Treynor, J. Lenihan, H. Jiang, M. Fleck, S. Bajad, G. Dang, D. Dengrove, D. Diola, G. Dorin, K. W. Ellens, S. Fickes, J. Galazzo, S. P. Gaucher, T. Geistlinger, R. Henry, M. Hepp, T. Horning, T. Iqbal, L. Kizer, B. Lieu, D. Melis, N. Moss, R. Regentin, S. Secrest, H. Tsuruta, R. Vazquez, L. F. Westblade, L. Xu, M. Yu, Y. Zhang, L. Zhao, J. Lievense, P. S. Covello, J. D. Keasling, K. K. Reiling, N. S. Renninger and J. D. Newman, *Nature*, 2013, **496**, 528–532.
54 J. Turconi, F. Griolet, R. Guevel, G. Oddon, R. Villa, A. Geatti, M. Hvala, K. Rossen, R. Göller and A. Burgard, *Org. Process Res. Dev.*, 2014, **18**, 417–422.
55 L. Feng, Y. Wang, S. Yuan, K.-Y. Wang, J.-L. Li, G. S. Day, D. Qiu, L. Cheng, W.-M. Chen, S. T. Madrahimov and H.-C. Zhou, *ACS Catal.*, 2019, **9**, 5111–5118.
56 Y. Wang, L. Feng, J. Pang, J. Li, N. Huang, G. S. Day, L. Cheng, H. F. Drake, Y. Wang, C. Lollar, J. Qin, Z. Gu, T. Lu, S. Yuan and H. C. Zhou, *Adv. Sci.*, 2019, **6**, 1802059.
57 M. A. Avery, W. K. M. Chong and C. Jennings-White, *J. Am. Chem. Soc.*, 1992, **114**, 914–919.
58 S. Triemer, K. Gilmore, G. T. Vu, P. H. Seeberger and A. Seidel-Morgenstern, *Angew. Chem., Int. Ed.*, 2018, **57**, 5525–5528.
59 Z. Amara, J. F. B. Bellamy, R. Horvath, S. J. Miller, A. Beeby, A. Burgard, K. Rossen, M. Poliakoff and M. W. George, *Nat. Chem.*, 2015, **7**, 489–495.
60 F. Levesque and P. H. Seeberger, *Angew. Chem., Int. Ed.*, 2012, **51**, 1706–1709.
61 J. Pang, Z. Di, J.-S. Qin, S. Yuan, C. T. Lollar, J. Li, P. Zhang, M. Wu, D. Yuan, M. Hong and H.-C. Zhou, *J. Am. Chem. Soc.*, 2020, **142**, 15020–15026.
62 V. Vil', I. Yaremenko, A. Ilovaisky and A. Terent'ev, *Molecules*, 2017, **22**, 117.
63 L.-K. Sy and G. D. Brown, *Tetrahedron*, 2002, **58**, 897–908.
64 L.-K. Sy and G. D. Brown, *Tetrahedron*, 2002, **58**, 909–923.
65 Z. Hasan, J. W. Jun and S. H. Jhung, *Chem. Eng. J.*, 2015, **278**, 265–271.
66 J. Jiang and O. M. Yaghi, *Chem. Rev.*, 2015, **115**, 6966–6997.
67 J. Chen, K. Li, L. Chen, R. Liu, X. Huang and D. Ye, *Green Chem.*, 2014, **16**, 2490–2499.
68 Q.-x. Luo, M. Ji, M.-h. Lu, C. Hao, J.-s. Qiu and Y.-q. Li, *J. Mater. Chem. A*, 2013, **1**, 6530.
69 X. Li, L. Huang, A. Kochubei, J. Huang, W. Shen, H. Xu and Q. Li, *ChemSusChem*, 2020, **13**, 5073–5079.

